Decadal ~~sea level~~ sea-level variability in the Australasian Mediterranean Sea

Patrick Wagner[1] and Claus W. Böning[1]

[1]GEOMAR Helmholtz Centre for Ocean Research Kiel, Kiel Germany

Correspondence: Patrick Wagner (pwagner@geomar.de)

Abstract.

Strong ~~, regional sea level~~ regional sea-level trends, mainly related to ~~basin–wide~~ basin-wide wind stress anomalies, have been observed in the western tropical Pacific over the last three decades. Analyses of regional sea level in the densely populated regions of the neighbouring Australasian Mediterranean Sea (AMS; also called Tropical Asian Seas) are hindered by its complex topography and respective studies are sparse. We used a series of global, ~~eddy permitting~~ eddy-permitting ocean models, including a ~~high–resolution~~ high-resolution configuration that resolves the AMS with $\frac{1}{20}°$ horizontal resolution, forced by a comprehensive atmospheric forcing product over ~~1958 − 2016~~ 1958–2016, to characterize the patterns and magnitude of decadal ~~sea level~~ sea-level variability in the AMS. The nature of this variability is elucidated further by sensitivity experiments with interannual variability restricted to either the momentum or buoyancy fluxes, building on an experiment employing a repeated-year forcing without interannual variability in all forcing components. Our results suggest that decadal fluctuations of ~~ENSO~~ El Niño-Souther Oscillation (ENSO) account for over 80% of the variability in all deep basins of the region, except for the central South China Sea (SCS). ~~PDO–related changes~~ Changes related to the Pacific Decadal Oscillation (PDO) are most pronounced in the shallow Arafura and Timor seas and in the central SCS. On average, buoyancy fluxes account for less than 10% of decadal SSH variability, ~~although~~ but this ratio is highly variable over time and can reach values of up to 50%. In particular, our results suggest that buoyancy flux forcing amplifies the dominant ~~wind stress driven~~ wind-stress-driven anomalies related to ENSO cycles. Intrinsic variability is mostly negligible except in the SCS, where it accounts for 25% of the total decadal SSH variability.

1 Introduction

~~Over the last three decades sea level~~ Between the early 1990s and mid 2010s sea-level trends of up to 10 mm yr^{-1}, which exceeds three times the global mean rate, were observed in the western tropical Pacific and found to be related to an intensification of the Pacific trade wind regime (Timmermann et al., 2010; Merrifield, 2011; Merrifield and Maltrud, 2011; McGregor et al., 2012; Merrifield et al., 2012; Moon and Song, 2013; Moon et al., 2013; Qiu and Chen, 2012). This strong ~~sea level~~ sea-level rise had severe consequences for the population of the ~~low–lying~~ low-lying islands in the region (Becker et al., 2012), whose inhabitants are regularly referred to as the first climate refugees. ~~Sea level~~ Sea-level changes in the western tropical Pacific received a lot of scientific attention. Despite the exposed position of many densely populated, coastal communities, this is not

true for the neighbouring areas of the Australasian Mediterranean ~~Seas (AMS). Strong~~ Sea (AMS; see Fig. 1 for an overview map of the study domain). For the period 1993–2009 strong trends of up to 9 mm yr^{-1} have been observed in the southwestern part of the region, but trends are not uniform across the many small seas of the region (Strassburg et al., 2015) and studies on regional ~~sea level~~ sea-level variability in the region are sparse.

30

The best studied area in the region ~~,~~ in terms of ~~sea level,~~ sea-level is the South China Sea (SCS). It is the largest marginal sea of the region. The central and northeastern deep parts of the basin show the largest amplitudes of interannual and decadal variability (Cheng and Qi, 2007), with trends of up to 8 mm yr^{-1} for the period 1993-2012 (Cheng et al., 2016). There is a broad consensus that ~~ENSO~~ El Niño-Souther Oscillation (ENSO) has a strong impact on interannual ~~sea level~~ sea-level variability (Cheng and Qi, 2007; Cheng et al., 2016; Rong et al., 2007; Wu and Chang, 2005; Fang et al., 2006; Peng et al., 2013).

35 Subsurface heat content anomalies are advected into the basin via the Luzon Strait (Cheng and Qi, 2007; Rong et al., 2007) and coastal Kelvin Waves advect anomalies, related to ENSO and possibly the ~~PDO~~Pacific Decadal Oscillation (PDO), from the tropical Pacific clockwise around the Philippines into the SCS (Liu et al., 2011; Zhuang et al., 2013; Cheng et al., 2016). Local wind stress curl, also related to ENSO, might amplify ~~the signal~~ these sea-level anomalies in the central SCS (Cheng et al., 2016). In contrast, ~~(Kleinherenbrink et al., 2017)~~Kleinherenbrink et al. (2017) did not find a strong impact of tropical

40 wind stress variability on ~~sea level~~ sea-level changes in the SCS.

~~Sea level~~ Sea-level variability in the southeastern part of the AMS, i.e. between Borneo and Australia, received much less attention. However, the area has been of great interest since it represents the only ~~low–latitude~~ low-latitude connection of ocean

45 basins (Sprintall et al., 2014) and acts as an upper pathway of the global overturning circulation (Gordon, 1986). The main circulation feature is the Indonesian Throughflow (ITF) that transports heat and freshwater from the Pacific into the Indian Ocean (Gordon, 2005). The ITF variability on interannual time scales is mostly a response to variations of the Pacific trade winds and governed by ~~large–scales climate indices~~large-scale climate modes. In particular, ENSO has a strong effect on ITF transport on interannual time scales (Meyers, 1996; Wijffels and Meyers, 2004; Liu et al., 2015). Decadal ITF variability is

50 also linked to shifts of the Pacific trade wind regime (Wainwright et al., 2008; Liu et al., 2010; Zhuang et al., 2013; Feng et al., 2011, 2015), but other mechanism, like deep Pacific upwelling (Feng et al., 2017), could also play a role. However, given the impact of Pacific easterlies on ITF variability, it is reasonable to assume that sea level along the ITF pathways is also remotely controlled by the Pacific trade wind regime. Indeed, ~~sea level~~ sea-level variability along the Australian west coast is closely linked to variability in the western tropical Pacific (Feng et al., 2004; Lee and McPhaden, 2008; Merrifield et al., 2012). This

55 requires a way for signals to cross the AMS. The theory of an equatorial waveguide, that allows remote forcing of variability in the throughflow region, was already proposed in 1994 (Clarke and Liu, 1994). Wijffels and Meyers (2004) ~~could show from XBT observations that sea level~~ showed, based on XBT observations from 1984 to 2001, that sea-level anomalies propagate from the Pacific Ocean along the Papuan and Australian shelf break into the Indian Ocean and that interannual variability is driven by remote wind forcing from the Pacific.
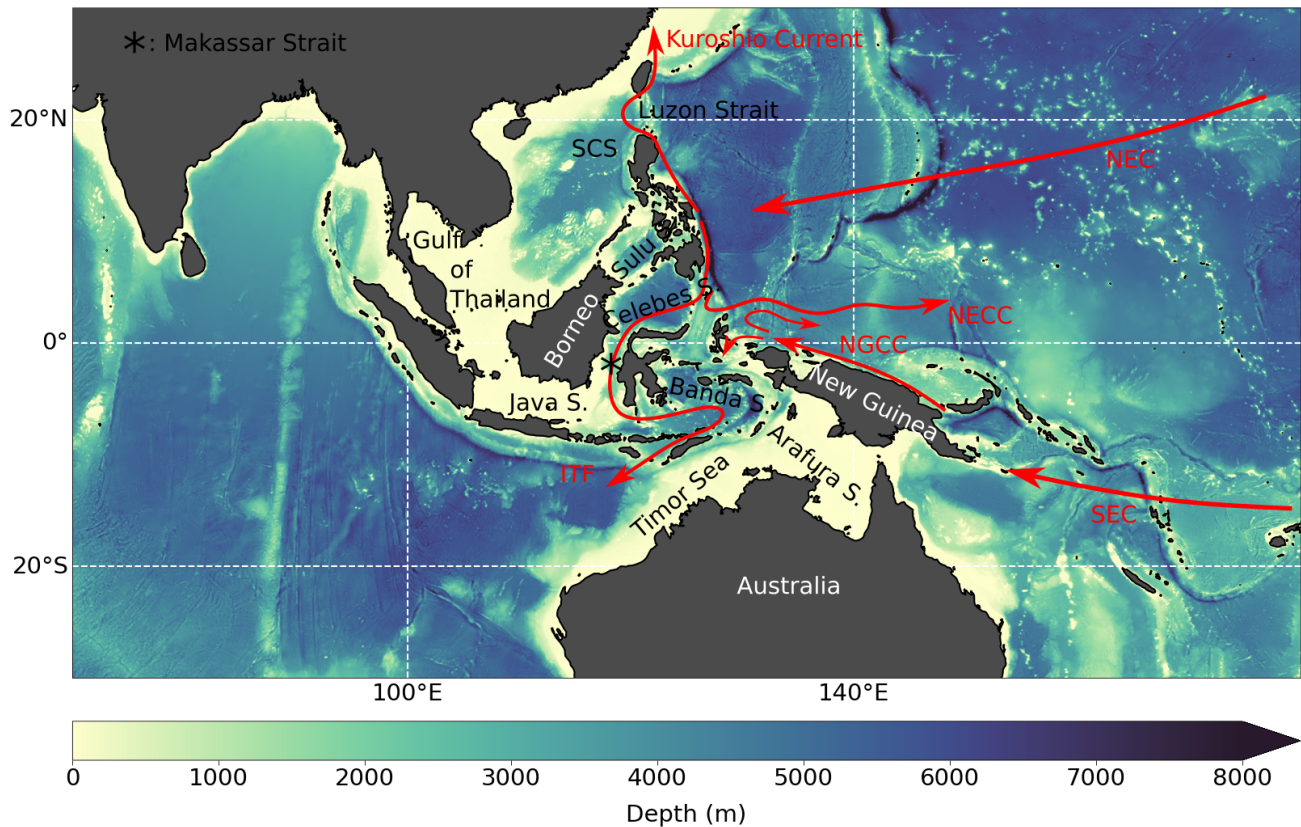
60

2

Figure 1. *Overview map of study domain, depicting the marginal seas and schematic currents discussed in the text. Colourshading indicates depth. Marginal seas, islands, continents and schematic currents that are mentioned in the text are also marked. SCS: South China Sea, NEC: North Equatorial Current, SEC: South Equatorial Current, NECC: North Equatorial Counter Current.*

In a more detailed analysis, Kleinherenbrink et al. (2017) separated observed ~~sea level~~ sea-level changes between 2005 and 2012 into mass and steric components. They found mass changes to be relevant in the shelf regions, where a shallow water column is unable to expand due to density changes. Furthermore, they reported that the deep basins of the Banda and Celeb seas show large steric ~~sea level~~ sea-level variability on interannual time scales which appear to be linked to wind stress anomalies over the tropical Pacific. Using the Dipole Mode Index (DMI; Saji et al. 1999) they also found an impact of the Indian Ocean that is however limited to the Timor Sea. Strassburg et al. (2015) could also link observed and reconstructed decadal ~~trends during the last 60 years to PDO–related~~ sea-level trends between 1950 and 2009 to PDO-related wind stress changes over the tropical Pacific.

Comparatively little is known about the importance of local or remote buoyancy fluxes that has been proven to be relevant for sea level in other parts of the world's ocean, including the tropical Pacific (e.g. Piecuch and Ponte 2011; Piecuch et al.

2019; Wagner et al. 2021). Cheng and Qi (2007) suggested an influence of ocean–atmosphere freshwater fluxes on halosteric sea level in the SCS. In particular, the observed decrease between 2001 and 2005 was found to coincide with a salinification trend due to reduced freshwater fluxes. Rong et al. (2007) pointed out that local precipitation anomalies are the primary control of the SCS-mass budget and thereby also influences sea level.

Using ocean and climate models to analyse sea level in this region is hindered by its complex topography that forms many small seas and narrow straits. For example, the Labani channel, the deep part of the Makassar strait and the main pathway of the ITF, is only about 40 km broad, which is barely resolved in an 1/4° ocean model, let alone in even coarser climate models. We therefore used a series of ocean model experiments that consists of two hindcast simulations that subject to realistic atmospheric forcing covering the last six decades and providing horizontal resolution of 1/4° and 1/20°, supplemented by a series of sensitivity experiments that allow an individual application of momentum and buoyancy flux forcing to the underlying ocean. The aim of this study is to examine the sea level sea-level variability in the AMS in high–resolution high-resolution ocean model simulations subject to atmospheric forcing over the last six decades. In particular, the objectives are:

– To elucidate the patterns and nature of the regional sea level sea-level variability on decadal to multi–decadal multi-decadal time scales, including the impacts of the low-frequency ENSO and PDO changes , which have been identified in previous studies as major drivers of sea level sea-level variability on interannual to decadal time scales.

– To examine the possible contribution of intrinsic variability, internally generated by ocean dynamics, to the total sea level sea-level variability in the region, and to determine the relative roles of momentum and buoyancy fluxes to the forced variability.

– To decompose steric sea level variability into its thermosteric and halosteric components to analyse their individual contributions. analyse the individual contributions of temperature and salinity changes to steric sea-level variability.

We used a series of ocean model experiments that consists of two realistic hindcast simulations covering the last six decades and providing horizontal resolution of 1/4° and 1/20°, supplemented by a series of sensitivity experiments that allow an individual application of momentum and buoyancy flux forcing to the underlying ocean.

Concerning the notation of the marginal seas between Australia and Asia, some deviating conventions have been used in the natural science community since international standards have not been officially updated since 1953 (International Hydrographic Organisation, 1953). Examples are "Tropical Asian Seas" (Kleinherenbrink et al., 2017), "Southeastern Asian Seas" (Strassburg et al., 2015) and "Australasian Mediterranean Sea" (AMS; Tomczak and Godfrey 2003). We adapted the latter for the purpose of this study and refer to all marginal seas in the region, including Timor and Arafura Seas and also the SCS, as AMS. It will be useful to point to the SCS and the remaining part of the region, individually. We use the term "Eastern Archipelagic Seas" (EAS) for this purpose.

2 ~~Model experiments~~Methods

2.1 Ocean general circulation model experiments

We used a global ocean model configuration of the "Nucleus for European Modelling of the Ocean" (NEMO) code version 3.6 (Madec and NEMO-team, 2016). The model employs a global ~~tri-polar~~ tri-polar ORCA grid and uses 46 vertical ~~z-levels~~ z-levels with varying layer thickness from 6 m at the surface to 250 m in the deepest levels. Bottom topography is represented by partial steps (Barnier et al., 2006) and is interpolated from ~~2-Minute~~ 2-Minute and 1-Minute Gridded Global Relief Data ETOPO2v2[1] and ETOPO1[2](Amante and Eakins, 2009) for the coarse and high-resolution experiments, respectively. The atmospheric forcing for all experiments is JRA55-do v1.3 (Tsujino et al., 2018) which builds on the JRA-55 reanalysis product but is specifically designed to be used as a forcing dataset for OGCMs. Most importantly, surface fields are corrected towards observations and heat and freshwater-fluxes are balanced with respect to a defined set of bulk formulas. Laplacian and bilaplacian operators were used to parameterize horizontal diffusion of tracer and momentum, respectively. The ocean model was coupled to the ~~Louvain-La-Neuve~~ Louvain-La-Neuve sea-ice model version 2 (LIM2-VP; Fichefet and Maqueda 1997). To avoid spurious drifts of global freshwater content, all models used a sea surface salinity restoring with piston velocities between 137 mm per day and 40 mm per day. The coarse resolution experiments additionally used a freshwater budget correction that sets changes in the global budget to zero at each model time step.

In order to increase the horizontal resolution in the area of interest, a ~~high-resolution~~ high-resolution "nest" was incorporated into the global base model. This approach allows a regional refinement of the horizontal resolution to $\frac{1}{20}°$ in the area from 50°S to 25°N and 75°E to 180°E. The nesting technique is based on the "adaptive grid refinement in fortran" (AGRIF; Debreu et al. 2008). A ~~two-way~~ two-way communication was established between the ~~high-resolution~~ high-resolution nest and the global "coarse" resolution model. The base model provided boundary conditions for the nest at every time step of the nest (the base model and the nest were integrated with a time step of 5 and 15 minutes, respectively). Due to the higher resolution of the nest in time and space, the boundary conditions were interpolated. The prognostic variables along the boundary of the nest were in turn updated after every time step of the base model by the calculations provided by the nest. Every three time steps, the full baroclinic state vector of the nest was averaged onto the base grid and fed back to the base model. This approach is well established, and the reader is referred for example to Schwarzkopf et al. (2019) for a detailed description of the procedure.

We integrated two reference configurations with interannually varying atmospheric forcing from 1958 to 2016:

- **REF005**: Reference run with $\frac{1}{4}°$ horizontal resolution globally and $\frac{1}{20}°$ in the nest area;

- **REF025**: Reference run with $\frac{1}{4}°$ horizontal resolution globally.

---

[1] http://www.ngdc.noaa.gov/mgg/global/relief/ETOPO2/ETOPO2v2-2006/ETOPO2v2g/, last access: 12 June 2018
[2] https://www.ncei.noaa.gov/access/metadata/landing-page/bin/iso?id=gov.noaa.ngdc.mgg.dem:316, last access: 11 October 2019

In addition, we followed the ~~recommendations of ?~~ approach of Stewart et al. (2020) to construct a "~~quasi–climatological~~quasi-climatolo

135 forcing. More specifically, we extracted ~~a 12–month~~ the recommended 12-month subset from May 1990 to April 1991 from the full forcing dataset and applied its individual fields repeatedly to suppress the interannual variability entirely or only for the computation of momentum or buoyancy fluxes, respectively. This way, we obtained three additional sensitivity experiments with $\frac{1}{4}°$ horizontal resolution globally, which were all integrated for 59 years to match the length of the reference configurations:

140 – **CLIM**: Full quasi-climatological forcing.

 – **WIND**: ~~Quasi–climatological~~ Quasi-climatological buoyancy fluxes.

 – **BUOY**: ~~Quasi–climatological~~ Quasi-climatological momentum fluxes.

The experiments WIND and BUOY are meant to isolate the ~~momentum forced and buoyancy forced~~ momentum-flux-forced and buoyancy-flux-forced variability. The approach builds on the assumption that the total ~~atmospherically–forced~~atmospherically-forced

145 variability can approximately be understood by a linear combination of these two contributions. Because we only suppress variability on interannual and longer timescales, this assumption is not valid for variability on shorter timescales. A possible deviation ~~from that could arise from intrinsic~~could also arise from non-linearities and intrinsic, i.e. unforced, ~~unforced~~ variability: an estimate of the magnitude of ~~its contribution will be provided by~~ the latter is provided by the experiment CLIM.

We note that the set of 1/4° ~~experiments~~ experiments (REF025, WIND, BUOY and CLIM) has been used previously for

150 studies of Indian Ocean heat content (Ummenhofer et al., 2020), marine heatwaves (Ryan et al., 2021) and tropical Pacific ~~sea level~~ sea-level variability (Wagner et al., 2021).

2.2 Observational datasets

We used two observational datasets to validate our model results. Satellite altimetry data is provided as a gridded product by the Copernicus Marine Environment Monitoring Service[3] (CMEMS) with a resolution of $\frac{1}{4}°$ that is available since 1993 (in

155 contrast to our model simulations that start in 1958). Observations of temperature and salinity were taken from the World Ocean Atlas 18[4] (WOA18; Locarnini et al. 2019; Zweng et al. 2019) that is also available with $\frac{1}{4}°$ horizontal resolution and covers the period from 1958 to 2017.

2.3 Steric sea level

Sea-level changes are either due to changes of the total mass of the water column or due to density changes of seawater. The

160 latter is referred to as steric sea level. Because seawater density is affected by temperature and salinity, steric sea level and can be separated into thermosteric and halosteric components, respectively. We diagnosed steric sea level changes from the stored

---

[3]https://resources.marine.copernicus.eu/?option=com_csw&view=details&product_id=SEALEVEL_GLO_PHY_L4_REP_OBSERVATIONS_008_047, last access: 12 June 2018

[4]https://www.ncei.noaa.gov/archive/accession/NCEI-WOA18, last access: 16 February 2021

model output:

$$\frac{\partial \eta_{steric}}{\partial t} = -\int_{-H}^{\eta} \frac{1}{\rho}\frac{\partial \rho}{\partial t}dz, \tag{1}$$

where (η) denotes sea level, ρ is seawater density and H is ocean depth. Thermosteric sea-level changes are given by:

$$\frac{\partial \eta_{thermosteric}}{\partial t} = \int_{-H}^{\eta} (\alpha\frac{\partial \Theta}{\partial t})dz, \tag{2}$$

where α is the thermal expansion coefficient and Θ is potential temperature. In the same way, halosteric sea level variations can be expressed:

$$\frac{\partial \eta_{halosteric}}{\partial t} = \int_{-H}^{\eta} (\beta\frac{\partial S}{\partial t})dz, \tag{3}$$

where β is the haline contraction coefficient and S is salinity.

3 Results

First, we ~~will~~ compare our model results to observational products for validation and to point out some resolution dependent biases. ~~Observations[5], provided by the Copernicus Marine Service Center,~~ Sea level observations from satellite altimetry show strong interannual sea surface height[5] (SSH) variability in the western tropical Pacific, off the east coast of the Philippines islands. Within the AMS, variability is most pronounced in the deep basins of the SCS and the adjacent Sulu, Celeb and Banda Seas as well as in the coastal regions of the Arafura and Timor Seas (Fig. ~~4 a~~1). Both hindcast simulations slightly underestimate the amplitude of standard deviations (SD) in particular in the western tropical Pacific by 1 to 2 cm (REF025 and REF005 respectively), but reproduce the spatial pattern well (Fig. ~~4~~2 b, c). The spatial average of SSH over the AMS (see black contour in Fig. ~~4~~2 c) reveals interannual to decadal variability. The latter is more pronounced in the ~~high-resolution~~ high-resolution configuration (REF005) and agrees well with the observed positive trends since the early 90s (Fig. ~~4~~2 d).

Figure 3 shows subsurface maps of mean fields and model biases of temperature and salinity ~~biases~~with respect to observations from WOA18, averaged over the upper 400 m, from both hindcast simulations. ~~The World Ocean Atlas 18 (WOA18; Locarnini et al. 2019; Z~~ ~~) will serve as an observational benchmark, and respective mean fields are also shown.~~ Both hindcasts exhibit some temperature biases, in particular in the tropical Pacific, where opposite signs right on the ~~equator~~ Equator and at about 8°N (Fig. 3

---

[5]~~GLOBAL OCEAN GRIDDED L4 SEA SURFACE HEIGHTS AND DERIVED VARIABLES REPROCESSED;~~ ~~https://resources.marine.copernicus.eu/?option=com_csw&view=details&product_id=SEALEVEL_GLO_PHY_L4_REP_OBSERVATIONS_008_047~~

[5]We will refer to the ~~sea level~~ sea-level estimate of the OGCMs, which gives height above the geoid, as SSH
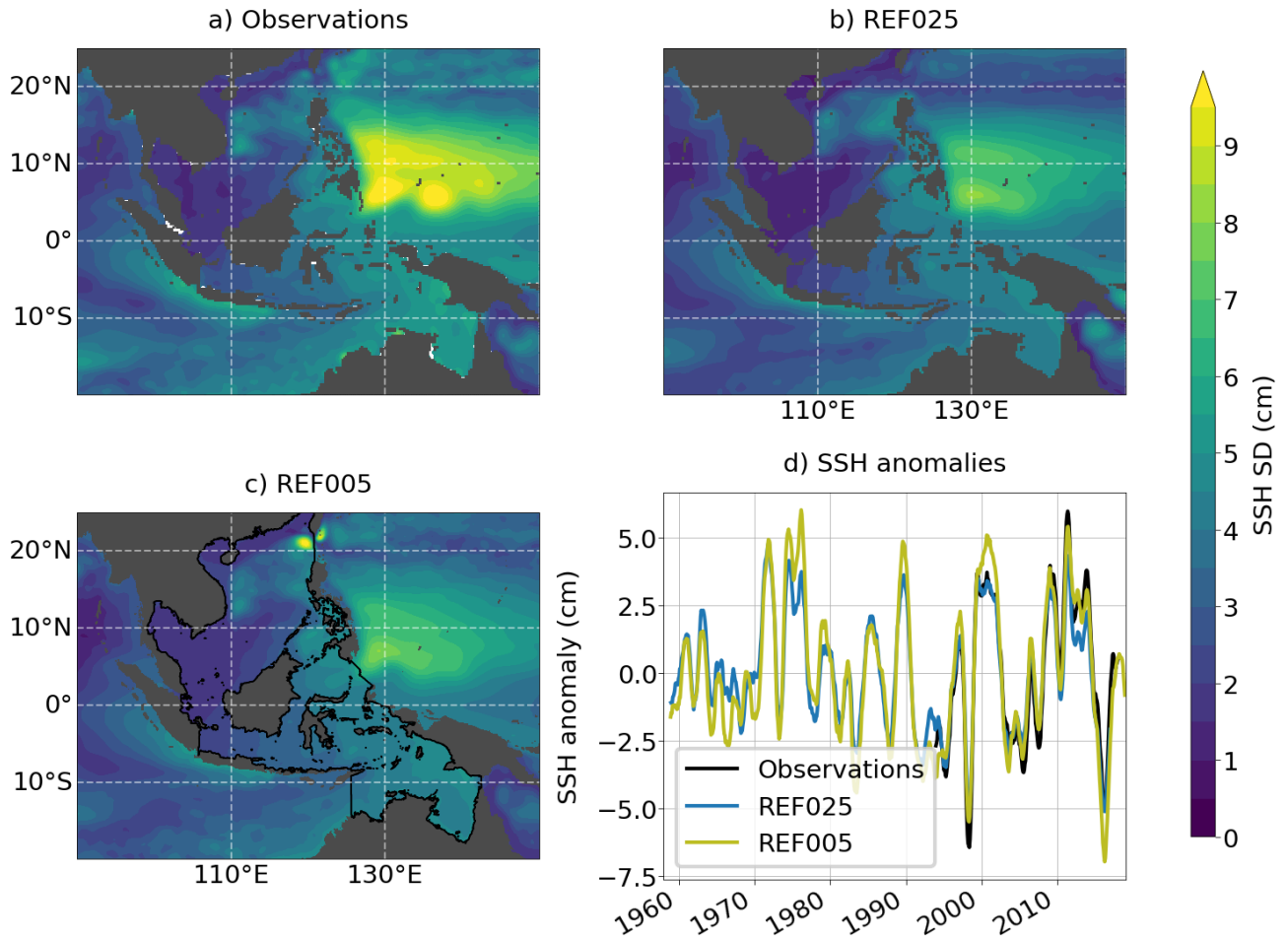
Figure 2. ~~Standard deviations (SD) of SSH from (a) observations and two hindcast experiments (b) REF025 and (c) REF005 over the period 1993 to 2016. d) SSH anomalies averaged over the region marked by black contours in panel c). SD is based on period from 1993 to 2016. The global mean trends have been subtracted, and all data was smoothed with a 12–month running mean window prior to calculation.~~ *SD of SSH from (a) observations and two hindcast experiments (b) REF025 and (c) REF005 over the period 1993 to 2016. d) SSH anomalies averaged over the region marked by black contours in panel c). The global mean trends over the integration period have been subtracted, and all data were smoothed with a 12-month running mean window.*

a–c) indicate a ~~large–scale~~ large-scale southward displacement of the Intertropical Convergence Zone (ITCZ) in the Pacific that causes a southward shift of the equatorial upwelling regime. The coarse resolution hindcast REF025 also shows positive temperature and salinity biases in the AMS. In particular in the northern part of the SCS, where values exceed 3°and 0.3 psu (Fig. 3 b, e). These biases are greatly reduced in the ~~high–resolution~~ high-resolution setup to temperature biases well below
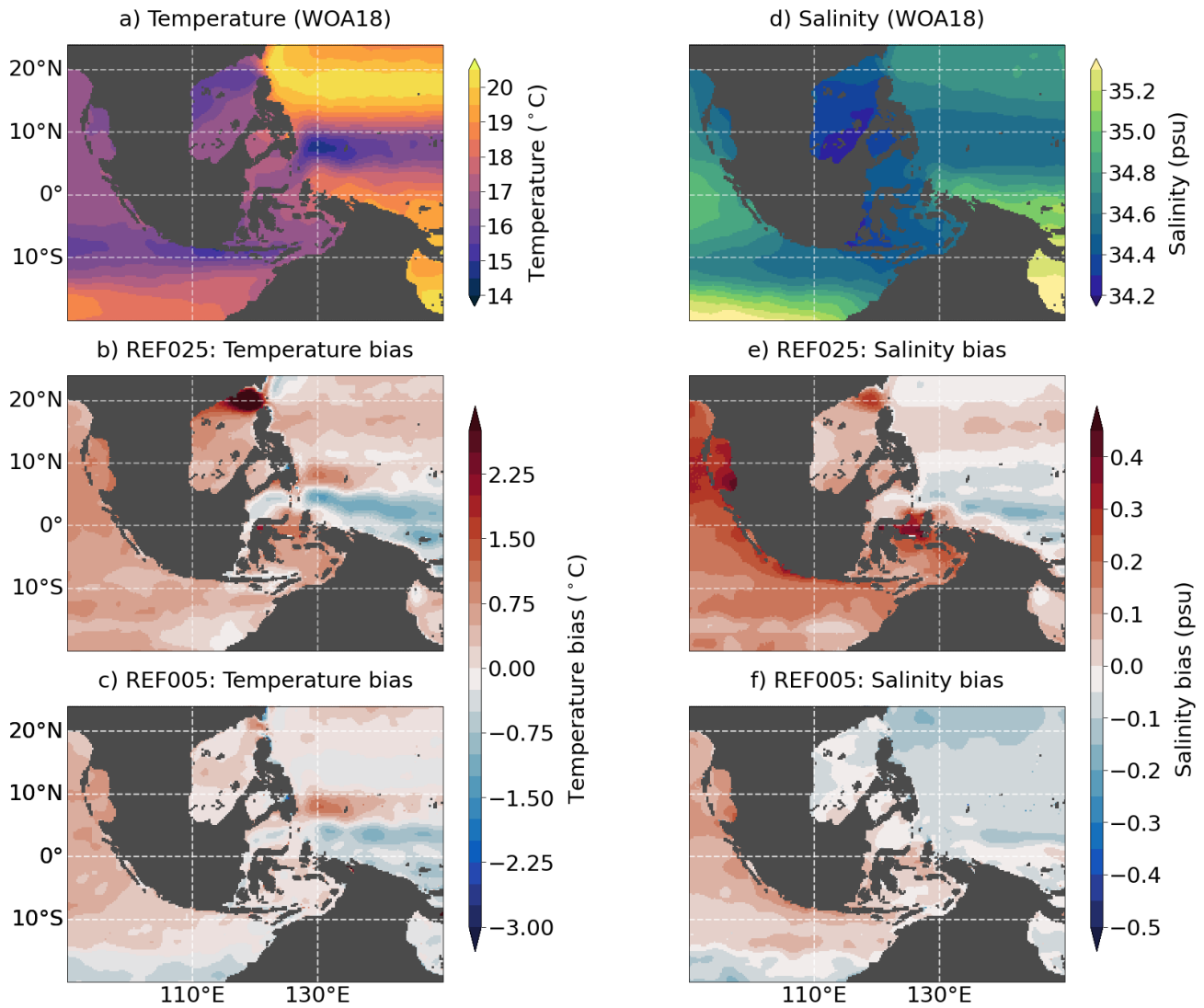
8

Figure 3. ~~Mean fields (upper row) and model biases (middle and bottom row) averaged over the upper 400 m for (a-c) temperature and (d-f) salinity.~~ *Mean fields (1955–2017; upper row) and model biases (1958–2016; middle and bottom row) averaged over the upper 400 m for (a-c) temperature and (d-f) salinity. Note that data is only shown where the water depth exceeds 400 m.*

0.5°C and salinity biases below 0.1 psu.

190

~~We will~~

3.1 Impact of buoyancy fluxes on SSH

We now turn to the forcing mechanism of decadal SSH variability and inspect the low-pass filtered (cutoff period of 8 years) SSH timeseries. Figure 4 presents maps of standard deviation (SD) for all five experiments, as well as SSH anomalies averaged over the AMS. The two hindcast simulations show a close resemblance in terms of amplitude and pattern, suggesting only a minor influence of the model resolution (Fig. 4 a, b). The pattern and amplitude of the WIND experiment (Fig. 4 c) closely match the signal in REF025, indicating that wind stress variability is the most important driver of the variability. The SSH signal driven by the interannual variability of buoyancy fluxes shows much lower amplitudes and a different spatial pattern (Fig. 4 d; note the different colorbars): it is most pronounced outside the AMS in the Kuroshio region and the southeastern, tropical Indian Ocean and within the AMS in the SCS, whereas values in the EAS are relatively low (about 0.4 cm).

While in most areas the total variability in REF025 can be understood as a linear superposition of variability due to momentum and buoyancy fluxes, this is not the case in the Kuroshio region or the Gulf of Thailand. Possible reasons are cancelling effects of out-of-phase variations of momentum and buoyancy fluxes or, as pointed out above, intrinsic ocean variability and non-linear effects. As evident from Fig. 4e), intrinsic variability in the AMS is below 0.2 cm everywhere except in the SCS. Amplitudes in the northern SCS reach values of up to 1 cm and are thereby comparable to the values of the buoyancy forcing experiment and account for about 25 % of the total variability in REF025.

Averaged over the AMS, buoyancy fluxes amplify the wind-stress-driven variability (Fig. 4 f). If we consider the change in variability between REF025 and WIND, rather than the variability in BUOY itself, to be the effect of buoyancy fluxes, we find a contribution of 9% (SD of 1.54 cm in REF025 and 1.4 cm in WIND) by which buoyancy fluxes amplify the wind stress-driven-variability. This fraction is however variable over time and reaches values of up to 50 %, for example during the late 1990s. When estimating the effect of buoyancy fluxes from BUOY directly, we obtain a much larger contribution of 24 %. The reason for this is intrinsic variability that is included in all experiments and adds to the variability in BUOY. We found no indication that buoyancy fluxes contribute to the increase in sea level between roughly 1990 and 2010 that is visible in both hindcast simulation and WIND.

3.2 Linear regression of SSH on ENSO and PDO indices

A linear regression model is used to quantify the impact of low-frequency ENSO changes and PDO cycles on sea-level variability. We use a band-pass filtered Niño3.4 index[6] (8–13 years) and a low-pass

---

[6]The Niño3.4 index is defined as the area averaged sea surface temperature (SST) anomaly in the Niño3.4 region (5° N–5° S, 170° W-120° W) with respect to the monthly climatology and normalized by its SD
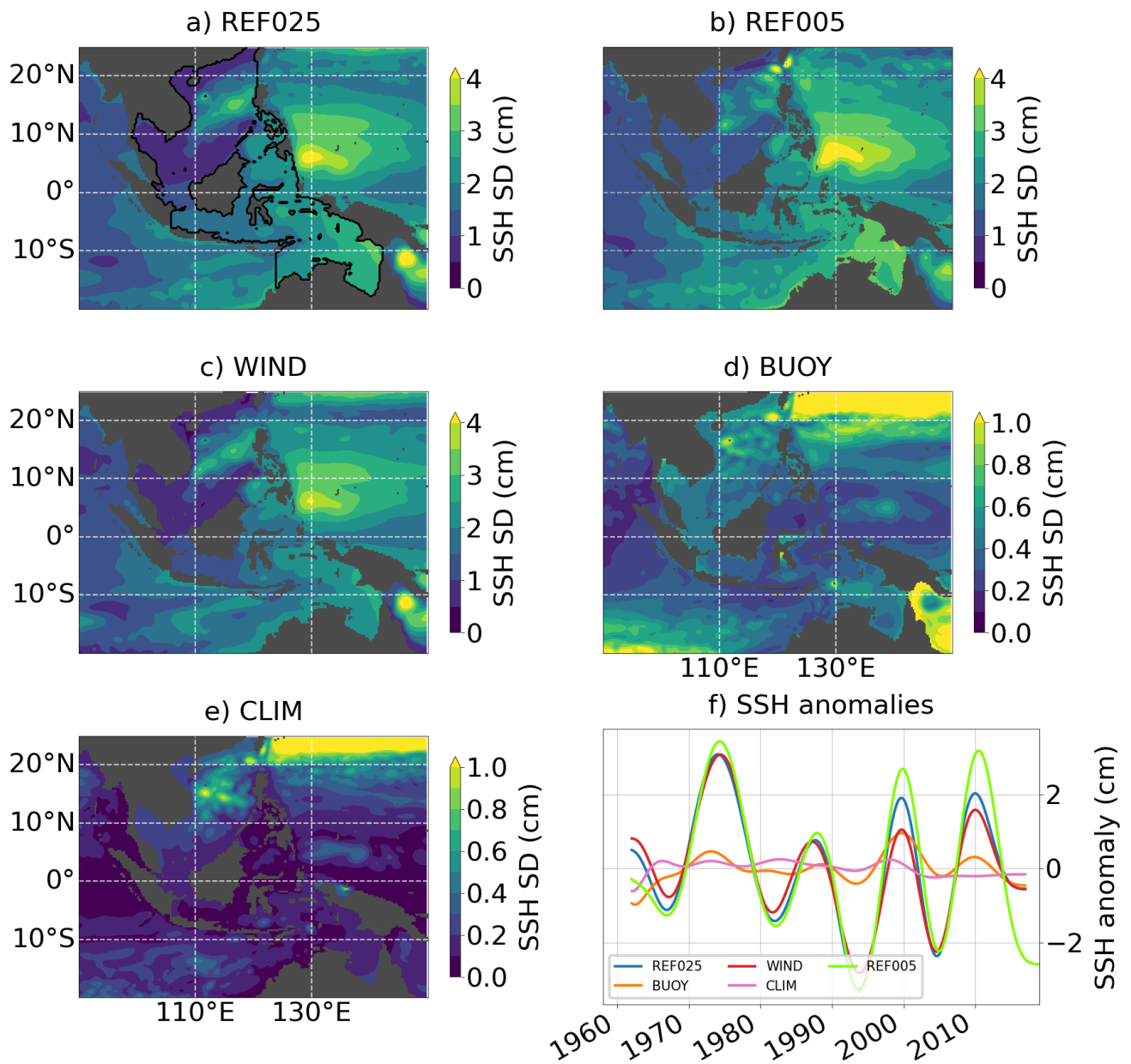
Figure 4. SD of low–pass filtered SSH timeseries (8 years) from (a) REF025, (b) REF005, (c) WIND, (d) BUOY, (e) CLIM and (f) low–pass filtered SSH anomalies averaged over black contour lines shown in panel a). Note the different colorbars. SD of low-pass filtered SSH timeseries (8 years) from (a) REF025, (b) REF005, (c) WIND, (d) BUOY, (e) CLIM and (f) low-pass filtered SSH anomalies averaged over black contour lines shown in panel a). Note the different colorbars.

filtered PDO low-pass filtered PDO[7] index (13 years) as predictors. Both indices are derived from REF025 and compare well with observational estimates (Fig. A1). Both indices are not significantly correlated (at a confidence interval of 5%) by construction because their variability is limited to time scales longer or shorter than 13 years. This allows a linear superposition of

225 the responses and their respective coefficients of determination (R^2 gives the fraction of variance explained by a linear model; e.g. Thomson and Emery 2014). As before, SSH data has been low-pass low-pass filtered (8 years) prior to the regression. Note that the PDO can be considered the low-frequency component of ENSO in this context to the extent that the PDO can be regarded as the low-frequency component of ENSO, an alternative, and largely equivalent separation could be build on the low-pass filtered Niño3.4 index instead of the PDO index. We will get back to this point in section 4. The Indian Ocean Dipole

230 Index (IOD; Saji et al. 1999) could account for possible impacts of the Indian Ocean. We do not include the IOD in our analysis because the index shows only very weak variability on the timescales considered here (not shown).

Figure 5 depicts the linear responses of SSH from three experiments to the Niño3.4 and PDO indices. Since its results are very similar to REF025, we omit the WIND case here but defer it to the appendix (Fig. A2). REF025 and REF005 show a sim-

235 ilar response to positive ENSO cycles (Fig. 5a, b). Strong negative anomalies in the western tropical Pacific with amplitudes of 4 cm off the east coast of the Philippines islands leak into the north-eastern north-eastern part of the SCS and also follow the equatorial wave guide across the Celebes and Banda seas and along the Australian shelf break into the Indian Ocean. Here, both hindcasts find amplitudes between 1 and 2 cm (Fig. 5 a, b). This pattern is mostly determined by wind stress variability, as the wind stress experiment shows similar results (Fig. A2) and the pattern in BUOY differs strongly (Fig. 5 c). Here, SSH

240 shows a weak but non-negligible non-negligible, negative response to ENSO cycles which is uniform across the domain and thereby amplifies the wind stress driven wind-stress-driven response by about 0.2 – 0.3 –0.3 cm in most parts of the region. Buoyancy fluxes counteract the wind stress driven wind-stress-driven variability off the northwest northeast coast of Australia, to the south of Papua New Guinea, such that the effective ENSO related SSH variability is almost zero.

245 The linear response to the PDO index shows strong amplitudes of 3 to and 4 cm (in REF005 and REF025 respectively; Fig. 5 d, e) to the east of Papua New Guinea in the region of the South Pacific Convergence Zone (SPCZ). Anomalies stretch northwestward along the shelf (Fig. 5 d, e) and into the EAS, in particular into the Arafura seas, with values between 1 and 2 cm. Both hindcast experiments also suggest an PDO-imprint a PDO-imprint in the Java seas and the central SCS. Again, the variability is mostly driven by momentum fluxes momentum-fluxes (Fig. A2). Buoyancy fluxes can not explain the dominant

250 pattern and tend to dampen the variability regionally. In particular in the SPCZ, but also in the western tropical Pacific north of 10°N, in the northern part of the SCS and in the Sulu Sea. The response in the remaining regions is mostly below 0.1 cm.

In order to determine what fraction of the total variability can be explained by these two climate indices, Fig. 6 displays R^2. Both hindcasts (and also the WIND experiment; Fig. A2 a) agree that ENSO determines a large fraction of the low-frequency

---

[7]The PDO index is obtained via an Empirical Orthogonal Function of monthly SST anomalies in the Pacific north of 20° N and defined as the leading mode of variability. The climatological annual cycle is subtracted to remove long-term trends.

low-frequency variability in the western tropical Pacific at around 5°N and in all deep basins with values of over 80 % and, to a slightly lesser extent, also in the Timor Sea and along the Australian shelf break. This fraction is reduced to less than 50 % for the buoyancy flux related variability (Fig. 6 c).

Both hindcast simulations find that over 50 % of the total decadal SSH variability in the SPCZ and the Java Sea and over 30 % in the central SCS can be explained by PDO cycles. Both differ in their estimate of the quantitative importance of the PDO for the remaining region of the EAS, but still find 10–20 % of explained variance in case of REF005 and even more in REF025. Note, however, that REF025 showed temperature and salinity biases in this region that might be the reasons for these discrepancies. The PDO does not drive any buoyancy-flux-driven SSH variability in the AMS (Fig. 6 f). The linear combination of both indices (not shown) gives high scores of over 80% throughout the domain except in the central and southern part of the SCS where intrinsic variability is relevant.

In order to understand the mechanisms which shape the sea level

3.3 Decomposition of SSH variability into thermosteric and halosteric contributions

To further elucidate the mechanisms shaping the sea-level signal, it is useful to analyse the dynamical response and also decompose the sea-level signal into its steric components. We neglect sea-level anomalies due to mass fluctuations because their relative contributions are small everywhere except on shelf regions (not shown; e.g. Forget and Ponte 2015) where the total variability is weakest.

As expected, the dynamical response to the ENSO cycles (Fig. 7 a-c) is governed by anomalies of the North Equatorial Counter Current at 4°N and by thermosteric SSH anomalies of over 4 cm in the western tropical Pacific. The latter change the inter-basin pressure gradient between the Pacific and the Indian Ocean. Specifically, a positive ENSO cycle leads to a reduction in SSH, which causes a decreased pressure gradient across the AMS. Consequently, northward velocity anomalies in the Makassar Strait and Banda Sea indicate a reduction of ITF transport. Steric changes are consistent with this dynamical response of the upper ocean. The reduction of the ITF transport causes a reduction in heat and freshwater transport from the western tropical Pacific through the EAS, which causes negative thermosteric and halosteric SSH anomalies along the ITF pathway. In particular in the Banda Sea and Timor Sea, halosteric anomalies complement the thermosteric signal and make a relevant contribution (∼1 cm) to the total signal of over 2 cm. Note, however, that thermosteric anomalies seem to originate from the warm pool region in the western tropical Pacific whereas halosteric anomalies are most pronounced in the EAS and the ITF outflow region in the Indian Ocean. This aspect is elaborated further two paragraphs below. Another question concerns the possibility of an asymmetric response to positive and negative ENSO phases. From an analysis of their individual contributions, we find that almost all regions with a non-negligible response to ENSO are characterized by similar amplitudes of SSH variability during
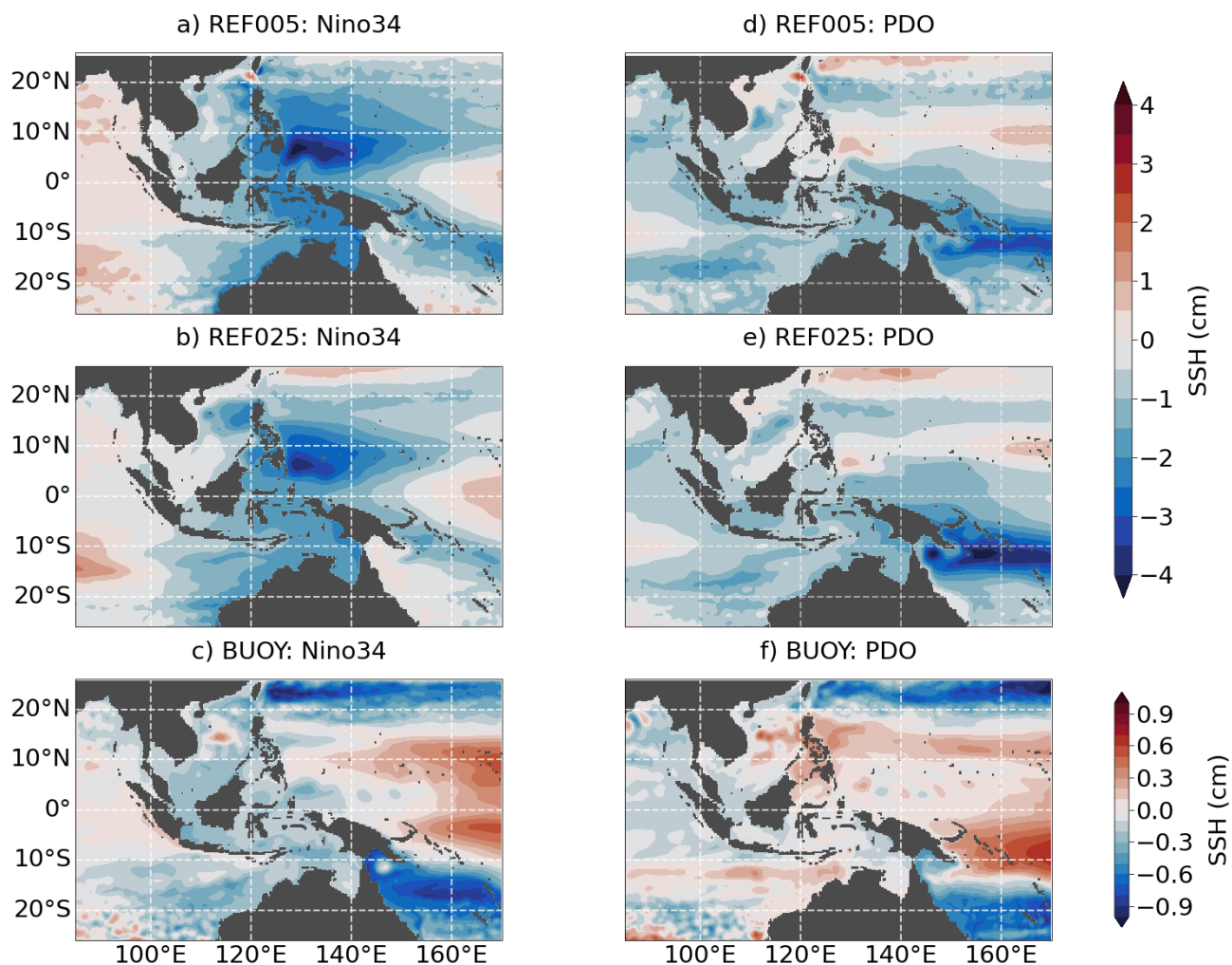
Figure 5. *Linear regression of SSH to (a-c) Niño3.4 index and (d-f) PDO index for two hindcast (REF025, REF005) and buoyancy forcing experiments (BUOY). Climate indices are derived from its base model in case of REF005 and from REF025 for the other two experiments. All data has been filtered with an 8–year low–pa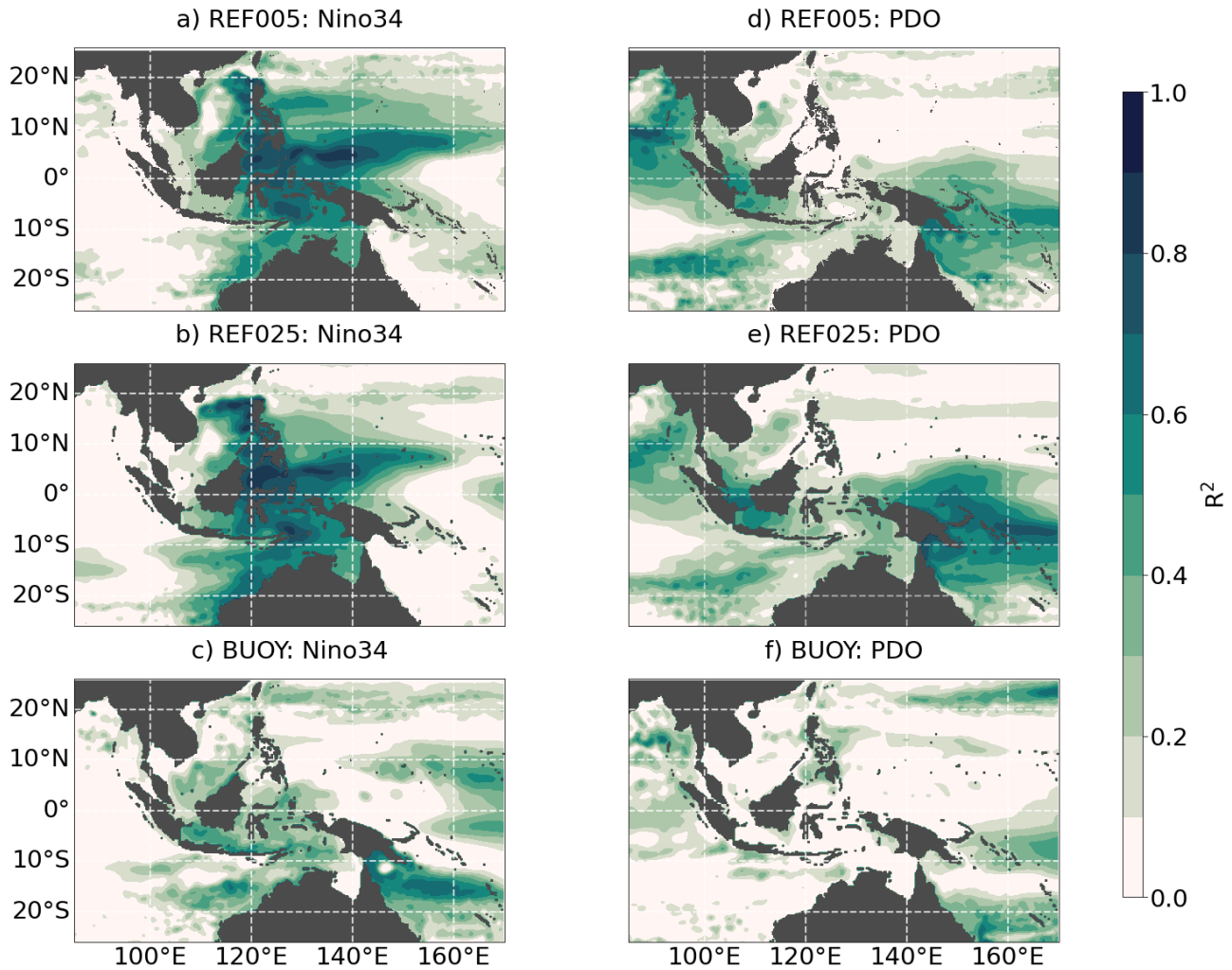ss filter. Note the different colorbars.Linear regression of SSH with (a-c) Niño3.4 index and (d-f) PDO index for two hindcast (REF025, REF005) and buoyancy forcing experiments (BUOY). Climate indices are derived from its base model in case of REF005 and from REF025 for the other two experiments. All data has been filtered with an 8-year low-pass filter. Note the different colorbars.*

Figure 6. *Coefficient of determination for the linear regression of SSH to (a-c) Niño3.4 index and (d-f) PDO index for two hindcast (REF025, REF005) and buoyancy forcing experiments (BUOY). Climate indices are derived from its base model in case of REF005 and from REF025 for the other two experiments. All data has been filtered with an 8-year low-pass filter.* *Coefficient of determination for the linear regression of SSH with (a-c) Niño3.4 index and (d-f) PDO index for two hindcast (REF025, REF005) and buoyancy forcing experiments (BUOY). Climate indices are derived from its base model in case of REF005 and from REF025 for the other two experiments. All data has been filtered with an 8-year low-pass filter.*

both phases. Only the Arafura Sea responds stronger to the negative cycle (not shown).

PDO related changes are dominated by anomalies of the South Equatorial Current and the ~~well known~~ well-known SSH changes in the SPCZ region (Fig. 7 d-f). Negative SSH anomalies during a positive PDO cycle are due to thermosteric anomalies, which are partly compensated by halosteric contributions. Negative anomalies change the pressure gradient along the coast of New Guinea and weaken the equatorward transport of warm and saline South Pacific waters via the New Guinea Coastal Current. This produces unfavourable conditions for South Pacific waters to enter the EAS, where we find negative thermosteric anomalies that are partly compensated by positive halosteric anomalies, similar to the changes in the SPCZ.

The compensating effect of temperature and salinity changes during PDO cycles ~~does also manifest~~ also manifests in the vertical profiles of temperature and salinity in the AMS. Figure 8 shows linear regressions of T and S averaged over the Banda Sea (7°S-3°S, 125°E 133°E: see red box in Fig. 7). Both ~~hindcast experiments~~ hindcast-experiments (Fig. 4a, b) indicate a strong, negative subsurface response (hence the density compensation) to positive PDO cycles. The ~~ENSO response~~ ENSO response is dominated by a subsurface temperature anomaly causing negative SSH values. The subsurface temperature anomalies during both ENSO and PDO cycles are amplified by sea surface salinity (SSS) anomalies. The two sensitivity experiments allow some insight into the origin of these surface signals (Fig. 4a, b). The momentum flux experiments (WIND) reproduces the subsurface signals, highlighting ~~their advective nature~~ the fact that they are due to wind-stress-driven advection, but shows no surface anomalies associated with ENSO and PDO cycles. These are instead driven by buoyancy fluxes. This fits the ~~ENSO related~~ ENSO-related halosteric anomalies (Fig. 7c) that do not seem to originate in the western tropical Pacific, but are instead forced by local buoyancy fluxes.

4 Summary and discussion

4.1 Summary

~~We used a series of global ocean model experiments to~~ We determine the characteristics of decadal ~~sea level~~ sea-level variability in the Australasian Mediterranean Sea and their relation to large scale climate modes of ENSO and PDO ~~.~~

by using a series of global ocean model experiments. Two reference configurations, that resolve the area of interest with $\frac{1}{4}°$ and $\frac{1}{20}°$ horizontal resolution, ~~were~~ are set up and forced with the newly developed JRA-55 do forcing (Tsujino et al., 2018). Both simulations are able to reproduce observed ~~sea level~~ sea-level variability in the western tropical Pacific and the AMS. We ~~found~~ find minor resolution dependent differences between both simulation in terms of SSH. However, the coarse resolution ~~configurations~~ configuration suffers from some upper ocean temperature and salinity biases, in particular in the northern part of the SCS and the Celebs Sea, which are alleviated in the ~~high resolution~~ high-resolution experiment.
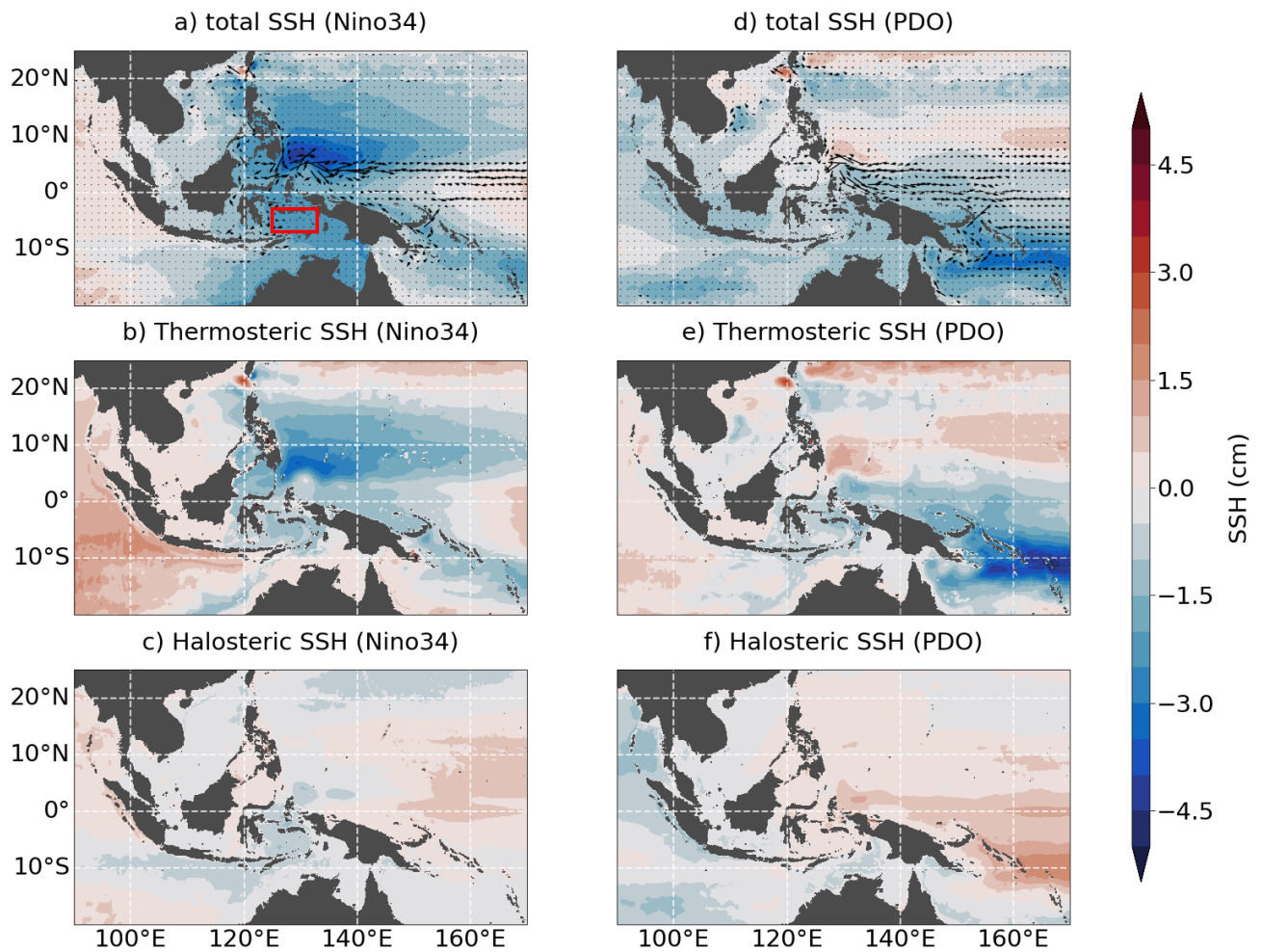
Figure 7. ~~Linear regression to (a-c) Niño3.4 and (d-f) PDO index of upper ocean currents (arrows; 0 − 150 m), total, thermosteric and halosteric SSH. All data is taken from REF005 and has been filtered with an 8–year low–pass filter.~~ *Linear regression with (a-c) Niño3.4 and (d-f) PDO index of upper ocean currents (arrows; 0–150 m), total, thermosteric and halosteric SSH. All data is taken from REF005 and were filtered with an 8-year low-pass filter. Note that the colour shading in panels a) and b) is the same as in Fig. 5a, b)*
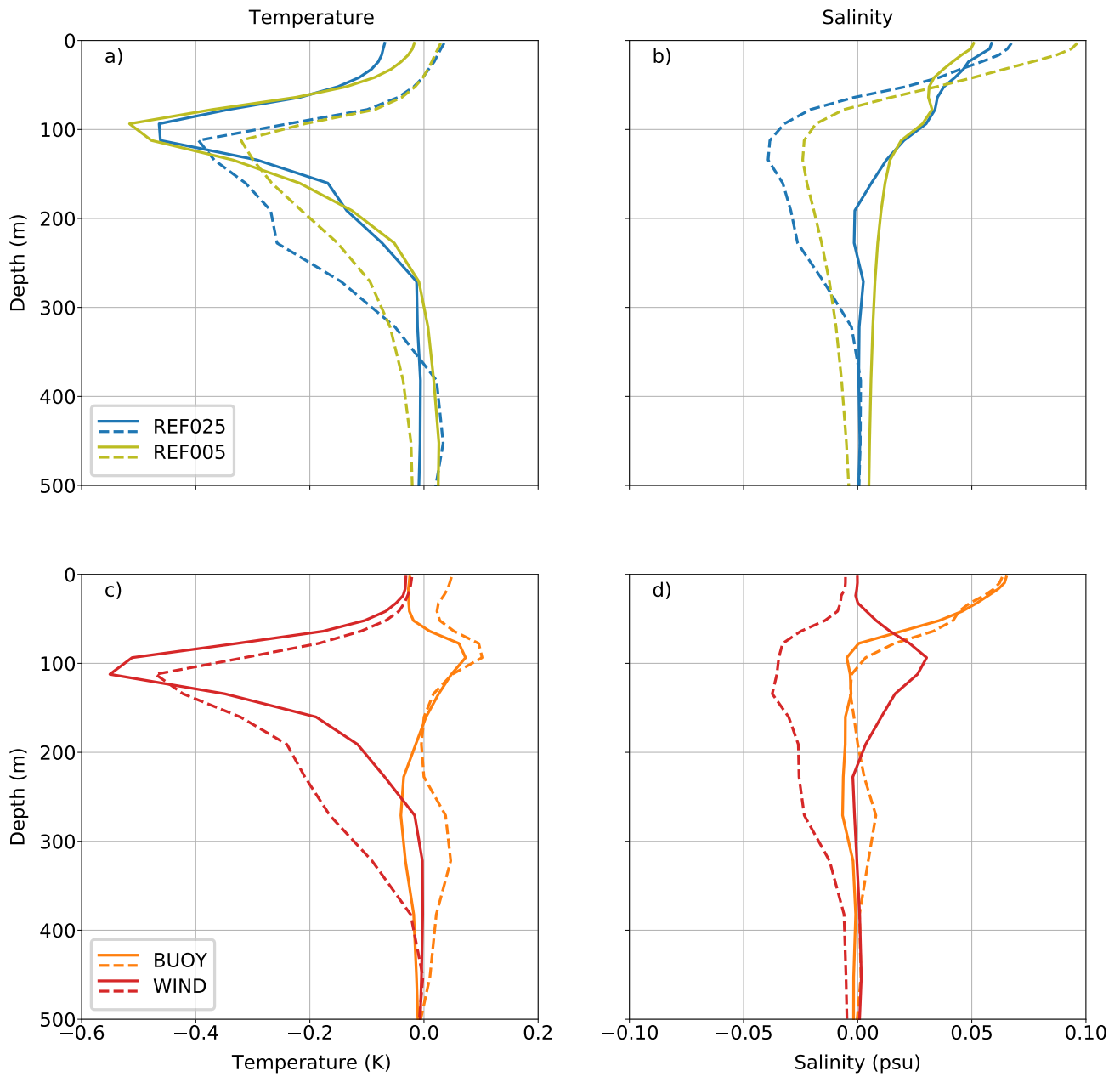
Figure 8. *Linear regression of temperature and salinity to Niño3.4 (solid) and PDO index (dashed) from (a, b) reference experiments and (c, d) sensitivity experiments. All data has been filtered with an 8-year low-pass filter.* Linear regression of temperature and salinity to Niño3.4 (solid) and PDO index (dashed) from (a, b) reference experiments and (c, d) sensitivity experiments. All data has been filtered with an 8-year low-pass filter.

320   We ~~assessed~~ assess the regional fingerprints of ENSO and PDO on SSH in the region. Both climate modes produce strong ~~sea level~~ sea-level signals in the western tropical Pacific. The ~~ENSO–related~~ ENSO-related signal is most pronounced just north of the ~~equator~~ Equator south of 10°N, which is in line with previous studies (e.g. Meng et al. 2019; Han et al. 2019). These strong SSH signals cause geostrophic flow anomalies as they change the ~~inter–basin~~ inter-basin pressure gradient between the Pacific ~~in~~ and the Indian Ocean and weaken the ITF (Hu et al., 2015). The imprint of the PDO in the northern part of the warm

325   pool is weak and instead shifted southward. ~~Again, this~~ This confirms earlier reports which found the effect of the PDO (on multidecadal time scales) in the western tropical Pacific to be most pronounced in the region of the SPCZ (Han et al., 2019; Moon et al., 2013; Becker et al., 2012). Our results suggest a partial compensation of thermo- and halosteric ~~PDO–related~~ PDO-related SSH anomalies. This is also in accordance with previous studies, which report a cooling and freshening of the southern part of the warm pool in response to a positive PDO cycle (Cravatte et al., 2009).

330

    Within the AMS itself we ~~found~~ find that, except for the central and northern SCS, over 80% of the variability in the deep basins of the AMS is determined by ~~low–frequency~~ low-frequency fluctuations of ENSO. The imprint of PDO cycles within the AMS is pronounced in the shallow Arafura/Timor and Java seas, where it explains 20% and 50% of the total variability, respectively. Analysing ~~sea level~~ sea-level trends since the early 90s from altimetry, tide gauge observations and reconstructions,

335   Strassburg et al. (2015) ~~found~~ find similar results with respect to the PDO. Furthermore, our results suggest distinctly different patterns of variability related to ENSO and PDO in the SCS, where the ENSO pattern is limited to the northeastern part, off the west coast of Luzon, and the PDO causes anomalies in the central SCS. This confirms previous results of idealized model studies (Cheng et al., 2016).

340   It can be expected that a clarification of the spatial pattern of multidecadal variability will aid future projections of sea level in the region. With the recent phase shift of the PDO, the affected regions should be primed for a weakening of the recent ~~sea level~~ sea-level rise, as it is also observed in the western tropical Pacific (e.g. Hamlington et al. 2016; Piecuch et al. 2019).

    In addition to two hindcast simulations, we set up a series of sensitivity experiments that used ~~quasi–climatological forcing (?)~~ quasi-climatological forcing (Stewart et al., 2020) to remove interannual variability from the full forcing or only from the

345   momentum or buoyancy fluxes.

    To our knowledge, the impact of buoyancy fluxes and intrinsic variability on regional sea level in the region has not been described in previous studies. Our results suggest that, even though momentum fluxes are the primary driver of variability, buoyancy fluxes are not negligible. According to our findings, they only contribute around 10% on average to the total variabil-

350   ity. However, this fraction is highly variable and can increase to up to 50% during ENSO cycles when they amplify the ~~wind stress driven sea level~~ wind-stress-driven sea-level anomalies. Indeed, buoyancy fluxes have been shown to be important for ~~sea level~~ sea-level variability in other regions, including the tropical Pacific (Piecuch and Ponte, 2012; Ponte, 2012; Wagner et al., 2021).

Intrinsic variability is relevant in the central SCS, where it accounts for 25% of the ~~low–frequency variability.~~low-frequency

355 variability.

4.2 Discussion

We did not investigate the origin of the high levels of intrinsic variability in the SCS in detail and can only speculate at this point. A connection to mesoscale variability and the ~~eddy active~~ eddy-active Kuroshio region, that also shows high levels of

360 intrinsic variability (Fig. 4 e), seems likely. Both regions are connected via the Luzon strait between Taiwan and the Philippines, and both regions show high levels of eddy kinetic energy (EKE; e.g. Scharffenberg and Stammer 2010). Besides local (Wang et al., 2008) and remote (Chen et al., 2009; Cheng and Qi, 2010) wind forcing, the Luzon strait transport (LST) has been identified in previous studies to drive interannual EKE variability in the SCS. An increased LST leads to a strengthening of the mean flow in the SCS, which creates favourable condition for baroclinic instabilities that allow a downscale energy transfer

365 (Sun et al., 2016). The strength of the LST is closely related to the Kuroshio current intrusion into the SCS (Qu et al., 2004; Wang and Fiedler, 2006) and the strength of the Kuroshio current itself. The Kuroshio current flows poleward along the western boundary, to which the Luzon Strait poses a gap through which the current can enter the SCS. The mechanism that control the pathways and strength of this intrusion are complex and remain controversial (Nan et al. 2015 and references therein), but also include mechanism by which eddies, generated by intrinsic variability in the Kuroshio region, impact the LST. While eddies

370 are unlikely to cross the Luzon Strait directly, they have been observed to modulate the strength of the Kuroshio current (Jie and De-Hai, 2010), which could be a means by which intrinsic variability from the Kuroshio region is indirectly communicated into the SCS. However, the viability of this hypothesis and the determination of the mechanism involved need to be addressed in future research.

375 The aim of this study ~~was~~ is to identify deterministic ~~low–frequency~~ low-frequency pattern of variability, associated with ~~large–scale~~ large-scale climate modes. Although the separation of climate indices along time scales (ENSO: 8–13 years; PDO: > 13 years) is somewhat arbitrary, the results ~~were not found to be~~ are not overly sensitive to the choice of the separation frequency. In fact, using only a ~~low–pass–filtered~~ low-pass filtered ENSO index (> 8 years) yields results that are similar to the combined effect of bandpass filtered ENSO and ~~low–pass~~ low-pass filtered PDO we presented here. ~~The~~ As already mentioned

380 above, the PDO can be understood as the ~~low–frequency~~ low-frequency component of ENSO in this context, and separating the time scales allowed us to show that the spatial pattern of SSH variability in the AMS, and the mechanisms that drive it, differ over these time scales.

An uncertainty of this study is the atmospheric forcing product used to drive the OGCMs. McGregor et al. (2012) ~~could~~

385 ~~demonstrate~~ demonstrated that most available atmospheric reanalyses, in conjunction with a linear shallow water model, are able to reproduce the ~~large–scale~~ large-scale pattern of SSH variability in the Pacific, and we can confirm this for the dataset used here. However, we find minor biases in both reference configurations that are most likely due to the forcing. Hsu et al.

(2021) ~~reported~~ report a wind stress curl bias in JRA55-do in the Pacific between 4–9° N that acts to diminish the meridional SSH gradient and flatten the SSH trough at this latitude. This is consistent with the warm bias we found at this latitudinal band.

Also, consistent with the results found here, they further ~~reported~~ report an underestimation of SSH trends between 1993 and 2007 in the western tropical Pacific ~~since the early 90s and related~~ and relate it to an underestimation of the observed trade wind intensification.

~~As a general conclusion it should be noted that the~~ A final point concerns the impact of model resolution in studies of variability patterns in this region. Although in our study we found only minor resolution-depended differences between the ~~1/4°- and 1/20°-configurations~~ $\frac{1}{4}$° and $\frac{1}{20}$°-configurations with respect to SSH signals, the stronger biases in the temperature and salinity ~~biases in the AMS emphasizes the need for very high model resolution to realistically capture~~ distributions seen in the coarser simulation should be taken as a reminder that a realistic representation of the dynamics of ~~this~~ the AMS area with its ~~intricate, small-scale bathymetry . A point of concern in this regard is that the coarser,~~ complex, small-scale bathymetry can require a very high model resolution. The importance of resolving the narrow straits and bathymetric details for capturing the ocean dynamics in the AMS was recently stressed in the review by Xue et al. (2020) of coupled ocean-atmosphere modelling for this region. In this context, it should be noted that the "coarse" 1/4°~~-grid size~~-grid used in this study ~~, represents the limit of current simulations of climate scenarios with coupled ocean–atmosphere~~ would rather be in the higher-resolution category of current climate simulations with coupled ocean-atmosphere models, suggesting that projections of regional ~~sea level~~ trend patterns in this area need to be interpreted with due caution. Downscaled projections (e.g., Sun et al., 2012; Feng et al., 2017), in which an uncoupled high-resolution OGCM is forced with a long-term climate change signal obtained from a climate model, might be a way to address this issue.
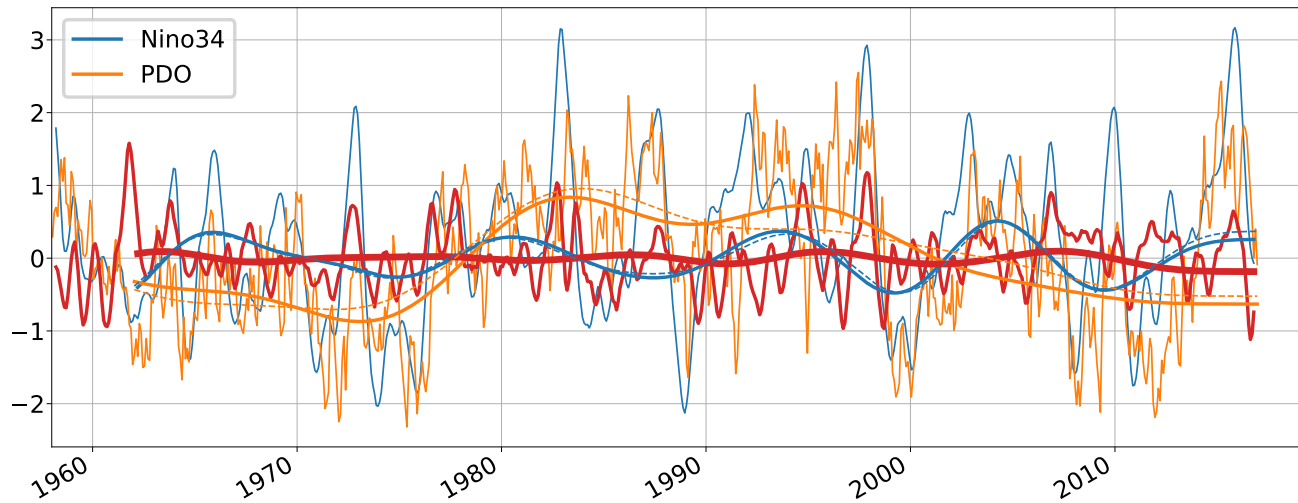
Figure A1. ~~*Niño3.4 index and PDO index, both calculated from REF025. Smoothed lines are band pass filtered with cutoff periods of 8 and 13 years (Niño3.4) and low–pass filtered with cutoff periods of 13 years (PDO).*~~*Niño3.4 index and PDO index, both calculated from REF025. Smoothed lines are band pass filtered with cutoff periods of 8 and 13 years (Niño3.4) and low-pass filtered with cutoff periods of 13 years (PDO). Dashed lines show observational estimates of the PDO index (http://research.jisao.washington.edu/pdo/PDO.latest, last access: 08 Jun 2017; Mantua et al. 1997) and the Niño3.4 index (https://psl.noaa.gov/gcos_wgsp/Timeseries/Data/nino34.long.data, last access: 07 Jun 2017; Rayner et al. 2003))*
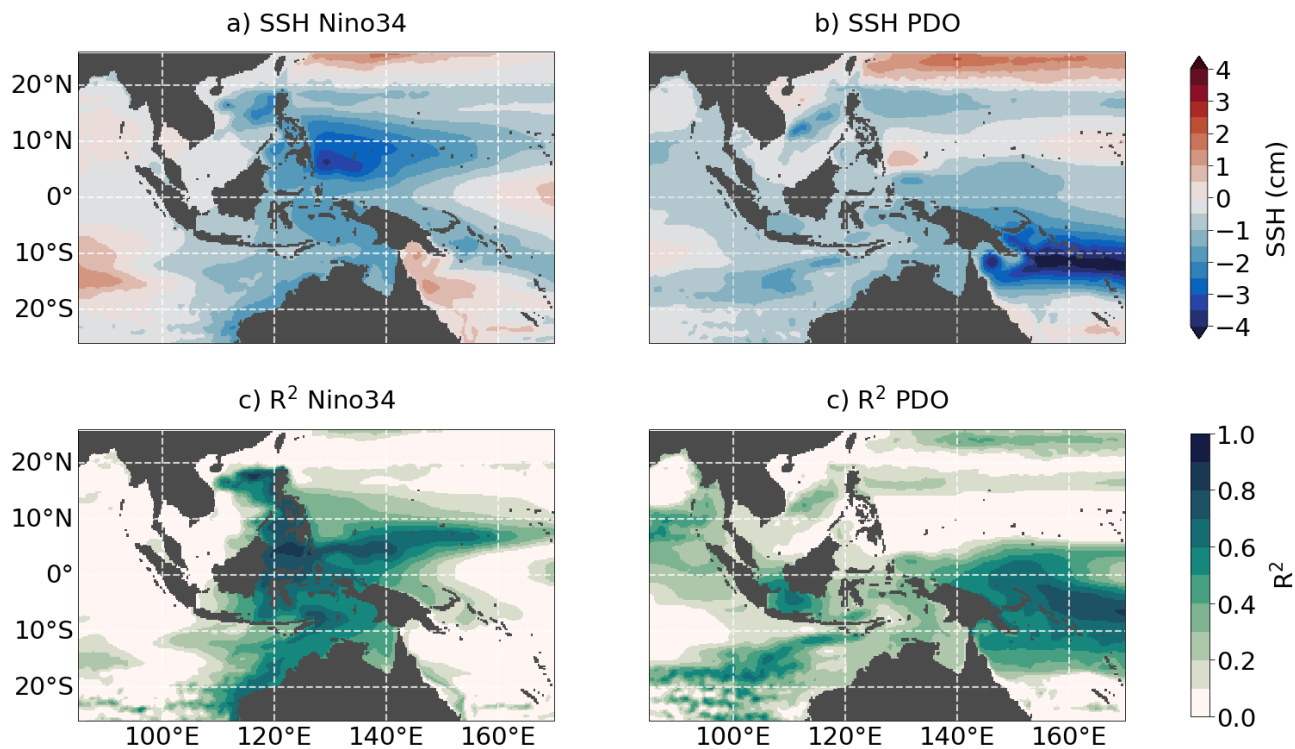
Figure A2. *Linear regression of SSH from WIND on (a) Niño3.4 and (b) PDO index and (c, d) respective coefficients of determination. Both climate indices are derived from REF025. All data has been filtered with an 8–year low–pass filter.*Linear regression of SSH from WIND on (a) Niño3.4 and (b) PDO index and (c, d) respective coefficients of determination. Both climate indices are derived from REF025. All data were filtered with an 8-year low-pass filter.

Author contributions. PW and CB defined the overall research problem and methodology; PW developed, ran, and validated the OGCM experiments ; PW produced all figures; PW prepared the paper with contributions from CB.

Competing interests. The authors declare that they have no conflict of interest.

References

Amante, C. and Eakins, B.: ETOPO1 1 Arc-Minute Global Relief Model: Procedures, Data Sources and Analysis. NOAA Technical Memorandum NESDIS NGDC-24., Tech. rep., National Geophysical Data Center, NOAA, https://doi.org/10.7289/V5C8276M, 2009.

Barnier, B., Madec, G., Penduff, T., Molines, J. M., Treguier, A. M., Le Sommer, J., Beckmann, A., Biastoch, A., Böning, C., Dengg, J., Derval, C., Durand, E., Gulev, S., Remy, E., Talandier, C., Theetten, S., Maltrud, M., McClean, J., and De Cuevas, B.: Impact of partial steps and momentum advection schemes in a global ocean circulation model at eddy-permitting resolution, Ocean Dynamics, 56, 543–567, https://doi.org/10.1007/s10236-006-0082-1, 2006.

Becker, M., Meyssignac, B., Letetrel, C., Llovel, W., Cazenave, A., and Delcroix, T.: Sea level variations at tropical Pacific islands since 1950, Global and Planetary Change, 80-81, 85–98, https://doi.org/10.1016/j.gloplacha.2011.09.004, 2012.

Boyer, T. P., García, H. E., Locarnini, R. A., Zweng, M. M., Mishonov, A. V., Reagan, J. R., Weathers, K. A., Baranova, O. K., Paver, C. R., Seidov, D., and Smolyar, I. V.: World Ocean Atlas 2018, https://www.ncei.noaa.gov/archive/accession/NCEI-WOA18, last access: 16 February 2021.

Chen, G., Hou, Y., Chu, X., Qi, P., and Hu, P.: The variability of eddy kinetic energy in the South China Sea deduced from satellite altimeter data, Chinese Journal of Oceanology and Limnology, 27, 943–954, https://doi.org/10.1007/s00343-009-9297-6, 2009.

Cheng, X. and Qi, Y.: Trends of sea level variations in the South China Sea from merged altimetry data, Global and Planetary Change, 57, 371–382, https://doi.org/10.1016/j.gloplacha.2007.01.005, 2007.

Cheng, X. and Qi, Y.: Variations of eddy kinetic energy in the South China Sea, Journal of Oceanography, 66, 85–94, https://doi.org/10.1007/s10872-010-0007-y, 2010.

Cheng, X., Xie, S. P., Du, Y., Wang, J., Chen, X., and Wang, J.: Interannual-to-decadal variability and trends of sea level in the South China Sea, Climate Dynamics, 46, 3113–3126, https://doi.org/10.1007/s00382-015-2756-1, 2016.

Clarke, A. J. and Liu, X.: Interannual Sea Level in the Northern and Eastern Indian Ocean, Journal of Physical Oceanography, 24, 1224–1235, https://doi.org/10.1175/1520-0485(1994)024<1224:ISLITN>2.0.CO;2, 1994.

CMEMS: Global Ocean Gridded L4 Sea Surface Heights and Derived Variables Reprocessed, https://resources.marine.copernicus.eu/?option=com_csw&view=details&product_id=SEALEVEL_GLO_PHY_L4_REP_OBSERVATIONS_008_047, last access: 12 June 2018.

Cravatte, S., Delcroix, T., Zhang, D., McPhaden, M., and Leloup, J.: Observed freshening and warming of the western Pacific Warm Pool, Climate Dynamics, 33, 565–589, https://doi.org/10.1007/s00382-009-0526-7, 2009.

Debreu, L., Vouland, C., and Blayo, E.: AGRIF: Adaptive grid refinement in Fortran, Computers and Geosciences, 34, 8–13, https://doi.org/10.1016/j.cageo.2007.01.009, 2008.

Fang, G., Chen, H., Wei, Z., Wang, Y., Wang, X., and Li, C.: Trends and interannual variability of the South China Sea surface winds, surface height, and surface temperature in the recent decade, Journal of Geophysical Research: Oceans, 111, 1–16, https://doi.org/10.1029/2005JC003276, 2006.

Feng, M., Li, Y., and Meyers, G.: Multidecadal variations of Fremantle sea level: Footprint of climate variability in the tropical Pacific, Geophysical Research Letters, 31, 2–5, https://doi.org/10.1029/2004GL019947, 2004.

Feng, M., Böning, C., Biastoch, A., Behrens, E., Weller, E., and Masumoto, Y.: The reversal of the multi-decadal trends of the equatorial Pacific easterly winds, and the Indonesian Throughflow and Leeuwin Current transports, Geophysical Research Letters, 38, 1–6, https://doi.org/10.1029/2011GL047291, 2011.

Feng, M., Benthuysen, J., Zhang, N., and Slawinski, D.: Freshening anomalies in the Indonesian throughflow and impacts on the Leeuwin Current during 2010-2011, Geophysical Research Letters, 42, 8555–8562, https://doi.org/10.1002/2015GL065848, 2015.

Feng, M., Zhang, X., Sloyan, B., and Chamberlain, M.: Contribution of the deep ocean to the centennial changes of the Indonesian Throughflow, Geophysical Research Letters, pp. 2859–2867, https://doi.org/10.1002/2017GL072577, 2017.

Fichefet, T. and Maqueda, M. A. M.: Sensitivity of a global sea ice model to the treatment of ice thermodynamics and dynamics, Journal of Geophysical Research: Oceans, 102, 12 609–12 646, https://doi.org/10.1029/97JC00480, 1997.

Forget, G. and Ponte, R. M.: The partition of regional sea level variability, Progress in Oceanography, 137, 173–195, https://doi.org/10.1016/j.pocean.2015.06.002, 2015.

Gordon, A. L.: Interocean exchange of thermocline water, Journal of Geophysical Research, 91, 5037–5046, https://doi.org/10.1029/jc091ic04p05037, 1986.

Gordon, A. L.: Oceanography of the Indonesian seas and their throughflow, Oceanography, 18, 15–27, https://doi.org/10.5670/oceanog.2005.01, 2005.

Hamlington, B. D., Cheon, S., Thompson, P. R., Merrifield, M. A., Nerem, R. S., Leben, R. R., and Kim, K.-Y.: An ongoing shift in Pacific Ocean sea level, Journal of Geophysical Research C: Oceans, 121, 5084–5097, https://doi.org/10.1002/2016JC011815, 2016.

Han, W., Stammer, D., Thompson, P., Ezer, T., Palanisamy, H., Zhang, X., Domingues, C. M., Zhang, L., and Yuan, D.: Impacts of Basin-Scale Climate Modes on Coastal Sea Level: a Review, Surveys in Geophysics, 40, 1493–1541, https://doi.org/10.1007/s10712-019-09562-8, 2019.

Hsu, C.-W., Yin, J., Griffies, S., and Dussin, R.: A Mechanistic Analysis of Tropical Pacific Dynamic Sea Level in GFDL-OM4 under OMIP-I and OMIP-II Forcings, Geoscientific Model Development Discussions, 14, 2471–2502, https://doi.org/10.5194/gmd-2020-374, 2021.

Hu, D., Wu, L., Cai, W., Gupta, A. S., Ganachaud, A., Qiu, B., Gordon, A. L., Lin, X., Chen, Z., Hu, S., Wang, G., Wang, Q., Sprintall, J., Qu, T., Kashino, Y., Wang, F., and Kessler, W. S.: Pacific western boundary currents and their roles in climate, Nature, 522, 299–308, https://doi.org/10.1038/nature14504, 2015.

International Hydrographic Organisation: Limits of Oceans and Seas, IMP, Monte-Carlo, 3 edn., hdl:10013/epic.37175.d001, 1953.

Jie, Z. and De-Hai, L.: Response of the Kuroshio Current to Eddies in the Luzon Strait, Atmospheric and Oceanic Science Letters, 3, 160–164, https://doi.org/10.1080/16742834.2010.11446856, 2010.

Kleinherenbrink, M., Riva, R., Frederikse, T., Merrifield, M., and Wada, Y.: Trends and interannual variability of mass and steric sea level in the Tropical Asian Seas, Journal of Geophysical Research: Oceans, 122, 6254–6276, https://doi.org/10.1002/2017JC012792, 2017.

Lee, T. and McPhaden, M. J.: Decadal phase change in large-scale sea level and winds in the Indo-Pacific region at the end of the 20th century, Geophysical Research Letters, 35, 1–7, https://doi.org/10.1029/2007GL032419, 2008.

Liu, Q., Wang, D., Zhou, W., Xie, Q., and Zhang, Y.: Covariation of the Indonesian Throughflow and South China Sea Throughflow Associated with the 1976/77 Regime Shift, Advances in Atmospheric Sciences, 27, 87–94, https://doi.org/10.1007/s00376-009-8061-3.1.Introduction, 2010.

Liu, Q., Feng, M., and Wang, D.: ENSO-induced interannual variability in the southeastern South China Sea, Journal of Physical Oceanography, 67, 127–133, https://doi.org/10.1007/s10872-011-0002-y, 2011.

490 Liu, Q.-Y., Feng, M., Wang, D., and Wijffels, S.: Interannual variability of the Indonesian Throughflow transport: A revisit based on 30 year expendable bathythermograph data, Journal of Geophysical Research: Oceans, 120, 6405–6418, https://doi.org/10.1002/2015JC011070.Received, 2015.

Locarnini, R. A., Mishonov, A. V., Baranova, O. K., Boyer, T. P., Zweng, M. M., Garcia, H. E., Reagan, J. R., Seidov, D., Weathers, K. W., Paver, C. R., and Smolyar, I. V.: World Ocean Atlas 2018, Volume 1: Temperature., Tech. rep., NOAA, Silver Spring, https:
495   //www.ncei.noaa.gov/sites/default/files/2021-03/woa18{_}vol1.pdf, 2019.

Madec, G. and NEMO-team: NEMO Ocean Engine, Tech. Rep. 27, Institut Pierre-Simon Laplace (IPSL), Paris, https://doi.org/10.5281/zenodo.1464816, 2016.

Mantua, N. J.: PDO Index, http://research.jisao.washington.edu/pdo/PDO.latest, last access: 08 June 2017.

Mantua, N. J., Hare, S. R., Zhang, Y., Wallace, J. M., and Francis, R. C.: A Pacific Interdecadal Climate Oscillation with
500   Impacts on Salmon Production, Bulletin of the American Meteorological Society, 78, 1069–1079, https://doi.org/10.1175/1520-0477(1997)078<1069:APICOW>2.0.CO;2, 1997.

McGregor, S., Gupta, A. S., and England, M. H.: Constraining wind stress products with sea surface height observations and implications for Pacific Ocean sea level trend attribution, Journal of Climate, 25, 8164–9176, https://doi.org/10.1175/JCLI-D-12-00105.1, 2012.

Meng, L., Zhuang, W., Zhang, W., Ditri, A., and Yan, X. H.: Decadal sea level variability in the Pacific Ocean: Origins and climate mode
505   contributions, Journal of Atmospheric and Oceanic Technology, 36, 689–698, https://doi.org/10.1175/JTECH-D-18-0159.1, 2019.

Merrifield, M. A.: A shift in western tropical Pacific sea level trends during the 1990s, Journal of Climate, 24, 4126–4138, https://doi.org/10.1175/2011JCLI3932.1, 2011.

Merrifield, M. A. and Maltrud, M. E.: Regional sea level trends due to a Pacific trade wind intensification, Geophysical Research Letters, 38, 1–5, https://doi.org/10.1029/2011GL049576, 2011.

510 Merrifield, M. A., Thompson, P. R., and Lander, M.: Multidecadal sea level anomalies and trends in the western tropical Pacific, Geophysical Research Letters, 39, 2–6, https://doi.org/10.1029/2012GL052032, 2012.

Meyers, G.: Variation of Indonesian Throughflow and the El Nino-southern oscillation, J. Geophys. Res, 101, 212–255, 1996.

Moon, J. H. and ~~Tony Song~~Song, Y. T.: Sea level and heat content changes in the western North Pacific, Journal of Geophysical Research: Oceans, 118, 2014–2022, https://doi.org/10.1002/jgrc.20096, 2013.

515 Moon, J. H., Song, Y. T., Bromirski, P. D., and Miller, A. J.: Multidecadal regional sea level shifts in the Pacific over 1958-2008, Journal of Geophysical Research: Oceans, 118, 7024–7035, https://doi.org/10.1002/2013JC009297, 2013.

Nan, F., Xue, H., and Yu, F.: Kuroshio intrusion into the South China Sea: A review, Progress in Oceanography, 137, 314–333, https://doi.org/10.1016/j.pocean.2014.05.012, 2015.

NOAA National Geophysical Data Center: ETOPO1 1 Arc-Minute Global Relief Model, https://www.ncei.noaa.gov/access/metadata/
520   landing-page/bin/iso?id=gov.noaa.ngdc.mgg.dem:316, last access: 11 October 2019, a.

NOAA National Geophysical Data Center: ETOPO2v2 2 Arc-Minute Global Relief Model, https://www.ngdc.noaa.gov/mgg/global/relief/ ETOPO2/ETOPO2v2-2006/ETOPO2v2g/netCDF/, last access: 12 June 2018, b.

NOAA/PSL: Nino34 Index, https://psl.noaa.gov/gcos_wgsp/Timeseries/Data/nino34.long.data, last access: 07 June 2017.

Peng, D., Palanisamy, H., Cazenave, A., and Meyssignac, B.: Interannual Sea Level Variations in the South China Sea Over 1950-2009,
525   Marine Geodesy, 36, 164–182, https://doi.org/10.1080/01490419.2013.771595, 2013.

Piecuch, C. G. and Ponte, R. M.: Mechanisms of interannual steric sea level variability, Geophysical Research Letters, 38, 1–6, https://doi.org/10.1029/2011GL048440, 2011.

Piecuch, C. G. and Ponte, R. M.: Buoyancy-driven interannual sea level changes in the southeast tropical Pacific, Geophysical Research Letters, 39, 1–5, https://doi.org/10.1029/2012GL051130, 2012.

530 Piecuch, C. G., Thompson, P. R., and Hamlington, B. D.: What Caused Recent Shifts in Tropical Pacific Decadal Sea-Level Trends ?, Journal of Geophysical Research: Oceans, 124, 7575–7590, https://doi.org/10.1029/2019JC015339, 2019.

Ponte, R. M.: An assessment of deep steric height variability over the global ocean, Geophysical Research Letters, 39, 1–5, https://doi.org/10.1029/2011GL050681, 2012.

Qiu, B. and Chen, S.: Multidecadal Sea Level and Gyre Circulation Variability in the Northwestern Tropical Pacific Ocean, Journal of
535 Physical Oceanography, 42, 193–206, https://doi.org/10.1175/JPO-D-11-061.1, 2012.

Qu, T., Kim, Y. Y., Yaremchuk, M., Tuzuka, T., Ishida, A., and Yamagata, T.: Can Luzon Strait transport play a role in conveying the impact of ENSO to the South China Sea?, Journal of Climate, 17, 3644–3657, https://doi.org/10.1175/1520-0442(2004)017<3644:CLSTPA>2.0.CO;2, 2004.

Rayner, N. A., Parker, D. E., Horton, E. B., Folland, C. K., Alexander, L. V., Rowell, D. P., Kent, E. C., and Kaplan, A.: Global analyses
540 of sea surface temperature, sea ice, and night marine air temperature since the late nineteenth century, Journal of Geophysical Research: Atmospheres, 108, https://doi.org/10.1029/2002jd002670, 2003.

Rong, Z., Liu, Y., Zong, H., and Cheng, Y.: Interannual sea level variability in the South China Sea and its response to ENSO, Global and Planetary Change, 55, 257–272, https://doi.org/10.1016/j.gloplacha.2006.08.001, 2007.

Ryan, S., Ummenhofer, C. C., Gawarkiewicz, G., Wagner, P., Scheinert, M., Biastoch, A., and Böning, C. W.: Depth structure of Ningaloo
545 Niño/Niña events and associated drivers, Journal of Climate, pp. 1767–1788, https://doi.org/10.1175/jcli-d-19-1020.1, 2021.

Saji, N. H., Goswami, B. N., Vinayachandran, P. N., and Yamagata, T.: A dipole mode in the tropical Indian Ocean, Nature, 401, 360–363, https://doi.org/10.1038/43854, 1999.

Scharffenberg, M. G. and Stammer, D.: Seasonal variations of the large-scale geostrophic flow field and eddy kinetic energy inferred from the TOPEX/Poseidon and Jason-1 tandem mission data, Journal of Geophysical Research: Oceans, 115, 1–29,
550 https://doi.org/10.1029/2008JC005242, 2010.

Schwarzkopf, F. U., Biastoch, A., Böning, C. W., Chanut, J., Durgadoo, J. V., Getzlaff, K., Harlaß, J., Rieck, J. K., Roth, C., Scheinert, M. M., and Schubert, R.: The INALT family - a set of high-resolution nests for the Agulhas Current system within global NEMO ocean/sea-ice configurations, Geoscientific Model Development Discussions, 12, 3329—-3355, https://doi.org/10.5194/gmd-12-3329-2019, 2019.

Sprintall, J., Gordon, A. L., Koch-Larrouy, A., Lee, T., Potemra, J. T., Pujiana, K., Wijffels, S. E., and Wij, S. E.: The Indonesian seas and
555 their role in the coupled ocean–climate system, Nature Geoscience, 7, 487–492, https://doi.org/10.1038/ngeo2188, 2014.

Stewart, K. D., Kim, W. M., Urakawa, S., Hogg, A. M. C., Yeager, S., Tsujino, H., Nakano, H., Kiss, A. E., and Dan-abasoglu, G.: JRA55-do-based repeat year forcing datasets for driving ocean–sea-ice models, Ocean Modelling, 147, 1–27, https://doi.org/10.1016/j.ocemod.2019.101557, 2020.

Strassburg, M. W., Hamlington, B. D., Leben, R. R., Manurung, P., Gaol, J. L., Nababan, B., Vignudelli, S., and Kim, K. Y.: Sea level trends
560 in Southeast Asian seas, Climate of the Past, 11, 743–750, https://doi.org/10.5194/cp-11-743-2015, 2015.

Sun, C., Feng, M., Matear, R. J., Chamberlain, M. A., Craig, P., Ridgway, K. R., and Schiller, A.: Marine downscaling of a future climate scenario for Australian boundary currents, Journal of Climate, 25, 2947–2962, https://doi.org/10.1175/JCLI-D-11-00159.1, 2012.

Sun, Z., Zhang, Z., Zhao, W., and Tian, J.: Interannual modulation of eddy kinetic energy in the northeastern South China Sea as revealed by an eddy-resolving OGCM, Journal of Geophysical Research: Oceans, 121, 3190–3201, https://doi.org/10.1002/2015JC011497.Received,
565 2016.

Thomson, R. ~~E. and Emery~~and Emery, W.: Data Analysis Methods in Physical Oceanography, Elsevier Science, 3 edn., 2014.

Timmermann, A., McGregor, S., and Jin, F. F.: Wind effects on past and future regional sea level trends in the southern Indo-Pacific, Journal of Climate, 23, 4429–4437, https://doi.org/10.1175/2010JCLI3519.1, 2010.

Tomczak, M. and Godfrey, J. S.: Regional Oceanography: an Introduction, Daya Publishing House, Delhi, 2 edn., 2003.

570 Tsujino, H., Urakawa, S., Nakano, H., Small, R. J., Kim, W. M., Yeager, S. G., Danabasoglu, G., Suzuki, T., Bamber, J. L., Bentsen, M., Böning, C. W., Bozec, A., Chassignet, E. P., Curchitser, E., Boeira Dias, F., Durack, P. J., Griffies, S. M., Harada, Y., Ilicak, M., Josey, S. A., Kobayashi, C., Kobayashi, S., Komuro, Y., Large, W. G., Le Sommer, J., Marsland, S. J., Masina, S., Scheinert, M., Tomita, H., Valdivieso, M., and Yamazaki, D.: JRA-55 based surface dataset for driving ocean–sea-ice models (JRA55-do), Ocean Modelling, 130, 79–139, https://doi.org/10.1016/j.ocemod.2018.07.002, 2018.

575 Ummenhofer, C. C., Ryan, S., England, M. H., Scheinert, M., Wagner, P., Biastoch, A., and Böning, C. W.: Late 20th Century Indian Ocean Heat Content Gain Masked by Wind Forcing, Geophysical Research Letters, 47, 1–10, https://doi.org/10.1029/2020GL088692, 2020.

Wagner, P.; Böning, C. W.: Supplementary Data to Decadal sea level variability in the Australasian Mediterranean Sea [Supplementary Dataset], hdl:20.500.12085/e300e837-c02e-4939-a9b6-a9be163cbd26, last access: 07 June 2021.

Wagner, P., Scheinert, M., and Böning, C.~~W.~~: Contribution of buoyancy fluxes to tropical Pacific sea level variability, Ocean Sci-580 ence~~Discussions preprint,~~, 17, 1103–1113, https://doi.org/https://doi.org/10.5194/os-17-1103-2021, 2021.

Wainwright, L., Meyers, G., Wijffels, S., and Pigot, L.: Change in the Indonesian Throughflow with the climatic shift of 1976/77, Geophysical Research Letters, 35, 1–5, https://doi.org/10.1029/2007GL031911, 2008.

Wang, C. and Fiedler, P. C.: ENSO variability and the eastern tropical Pacific: A review, Progress in Oceanography, 69, 239–266, https://doi.org/10.1016/j.pocean.2006.03.004, 2006.

585 Wang, G., Chen, D., and Su, J.: Winter eddy genesis in the eastern South China Sea due to orographic wind jets, Journal of Physical Oceanography, 38, 726–732, https://doi.org/10.1175/2007JPO3868.1, 2008.

Wijffels, S. and Meyers, G.: An Intersection of Oceanic Waveguides: Variability in the Indonesian Throughflow Region, Journal of Physical Oceanography, 34, 1232–1253, https://doi.org/10.1175/1520-0485(2004)034<1232:AIOOWV>2.0.CO;2, 2004.

Wu, C. R. and Chang, C. W.: Interannual variability of the South China Sea in a data assimilation model, Geophysical Research Letters, 32, 590 1–4, https://doi.org/10.1029/2005GL023798, 2005.

Xue, P., Malanotte-Rizzoli, P., Wei, J., and Eltahir, E. A.: Coupled Ocean-Atmosphere Modeling Over the Maritime Continent: A Review, Journal of Geophysical Research: Oceans, 125, 1–18, https://doi.org/10.1029/2019JC014978, 2020.

Zhuang, W., Qiu, B., and Du, Y.: Low-frequency western Pacific Ocean sea level and circulation changes due to the connectivity of the Philippine archipelago, Journal of Geophysical Research: Oceans, 118, 6759–6773, https://doi.org/10.1002/2013JC009376, 2013.

595 Zweng, M. M., Reagan, J. R., Seidov, D., Boyer, T. P., Antonov, J. I., Locarnini, R. A., Garcia, H. E., Mishonov, A. V., Baranova, O. K., Weathers, K. W., Paver, C. R., and Smolyar, I. V.: World Ocean Atlas 2018, Volume 2: Salinity, Tech. Rep. 82, NOAA, Silver Spring, 2019.